








Influence of Halide Choice on Formation of Low-Dimensional Perovskite Interlayer in Efficient Perovskite Solar Cells

Xueping Liu , Thomas Webb, Linjie Dai , Kangyu Ji, Joel A. Smith, Rachel C. Kilbride, Mozghan Yavari, Jinxin Bi, Aobo Ren, Yuanyuan Huang, Zhuo Wang , Yonglong Shen , Guosheng Shao* , Stephen J. Sweeney, Steven Hinder, Hui Li, David G. Lidzey, Samuel D. Stranks, Neil C. Greenham, S. Ravi P. Silva* , and Wei Zhang* 

Recent advances in heterojunction and interfacial engineering of perovskite solar cells (PSCs) have enabled great progress in developing highly efficient and stable devices. Nevertheless, the effect of halide choice on the formation mechanism, crystallography, and photoelectric properties of the low-dimensional phase still requires further detailed study. In this work, we present key insights into the significance of halide choice when designing passivation strategies comprising large organic spacer salts, clarifying the effect of anions on the formation of quasi-2D/3D heterojunctions. To demonstrate the importance of halide influences, we employ novel neo-pentylammonium halide salts with different halide anions (neoPAX, X=I, Br, or Cl). We find that regardless of halide selection, iodide-based (neoPA)₂(FA)_(n-1)Pb_nI_(3n+1) phases are formed above the perovskite substrate, while the added halide anions diffuse and passivate the perovskite bulk. In addition, we also find the halide choice has an influence on the degree of dimensionality (*n*). Comparing the three halides, we find that chloride-based salts exhibit superior crystallographic, enhanced carrier transport, and extraction compared to the iodide and bromide analogs. As a result, we report high power conversion efficiency in quasi-2D/3D PSCs, which are optimal when using chloride salts, reaching up to 23.35%, and improving long-term stability.

1. Introduction


Over the last decade, lead halide perovskite solar cells (PSCs) have emerged as a highly promising research direction in the field of photovoltaics. The excellent photovoltaic properties of the perovskite material combined with continuous optimization have enabled PSCs processing with certified power conversion efficiencies (PCEs) reaching up to 25.5%, comparable with the record PCE of the state-of-the-art crystalline silicon solar cells (26.7%).^[1,2] Despite the impressive progress made in producing high-quality polycrystalline films, further study on effective passivation strategies and the optoelectronic properties of the perovskite interfaces is still required to unlock the full potential of the perovskite devices.^[3–5] Among these, addressing the impact of defects through passivation has frequently been identified as essential for the development of high-performance PSCs.^[6]

Defects formed within the crystal structure, such as vacancies, interstitials, and antisites, can behave as nonradiative recombination centers

X. Liu, Y. Huang, Prof. Z. Wang, Dr. Y. Shen, Prof. G. Shao
State Center for International Cooperation on Designer Low-carbon & Environmental Materials (CDLCEM), Zhengzhou University, Zhengzhou 450001, China
E-mail: gsshao@zzu.edu.cn

X. Liu, T. Webb, Prof. M. Yavari, J. Bi, Dr. A. Ren, Prof. S. R. P. Silva, Dr. W. Zhang
Advanced Technology Institute, Department of Electrical and Electronic Engineering, University of Surrey, Guildford GU2 7XH, UK
E-mail: s.silva@surrey.ac.uk; wz0003@surrey.ac.uk
Dr. L. Dai, K. Ji, Dr. S. D. Stranks, Prof. N. C. Greenham
Cavendish Laboratory, University of Cambridge, Cambridge CB3 0HE, UK
Dr. S. D. Strank
Department of Chemical Engineering and Biotechnology, University of Cambridge, Cambridge CB3 0AS, UK
Dr. J. A. Smith, R. C. Kilbride, Prof. D. G. Lidzey
Department of Physics and Astronomy, University of Sheffield, Sheffield S3 7RH, UK

Dr. J. A. Smith
Department of Physics, University of Oxford, Clarendon Laboratory, Oxford OX1 3PU, UK
Prof. S. J. Sweeney
Advanced Technology Institute and Department of Physics, University of Surrey, Guildford GU2 7XH, UK
Dr. S. Hinder
The Surface Analysis Laboratory, Department of Mechanical Engineering Sciences, University of Surrey, Guildford GU2 7XH, UK
Prof. H. Li
Institute of Electrical Engineering, Chinese Academy of Sciences, Beijing 100190, China

 The ORCID identification number(s) for the author(s) of this article can be found under <https://doi.org/10.1002/eem2.12321>.

DOI: 10.1002/eem2.12321

and contribute to power losses within devices.^[7–9] Additionally, we now understand that defects can be mobile within the perovskite film, enabling migration through the lattice and accumulation at the interfaces, contributing to hysteresis phenomena.^[10,11] Moreover, the accumulated mobile defects states at the perovskite surfaces lead to pinning of the Fermi levels, screening the built-in voltage, and limiting the open-circuit voltage (V_{oc}).^[12,13] In addition to electrical performance, reactive defects at the perovskite interfaces have been heavily linked to the long-term stability of the PSCs, enabling pathways toward chemical degradation.^[14,15] Consequently, effective management of unexpected defects is essential for both device performance and environmental stability.

While the formation of point defects in solution-processed perovskite films is largely unavoidable, two strategies have been utilized to minimize their impact on PSC performance. Firstly, encouraging greater crystallinity and larger grains directly reduces the concentration of defect states that form in the bulk perovskite film.^[16–19] Secondly, where defects do occur, effective surface passivation can be used to suppress their destructive behavior.^[20–26] Recently, Kim *et al.* demonstrated that the addition of MACl to perovskite precursors had been linked to improved crystallinity of the resulting perovskite.^[27,28] Further tuning the precursor solution, Seok *et al.* highlighted that an excess of iodide ions within the perovskite film could reduce iodide vacancies, passivating deep iodine-based trap states.^[29,30] More recently, the addition of a secondary low-dimensional perovskite capping layer, comprising of larger organic spacer cations has stood out as an effective approach to passivation.^[26,31–33] The resulting low-dimensional perovskite phases, known as Ruddlesden–Popper (RP) phases, can be described with a general formula $A'_2A_{(n-1)}Pb_nX_{(3n+1)}$. The properties of RP phases are highly dependent on the n value, which corresponds to the number of inorganics $[BX_6]^{4-}$ octahedral layers stacked between two organic spacer molecules (A').^[34] As a consequence of the tunable dimensionality of RP phases, ambiguity exists over the dimensionality of the perovskite phases formed when using a post-treatment process. Recently, You *et al.* have suggested that in the absence of an annealing stage after the deposition of the organic salt solution, no RP phases are formed.^[20,35,36] While the tendency of low-dimensional phases to form under heating is becoming increasingly better understood, the influences on the n number of the secondary perovskite are less well understood. Conflicting arguments have previously suggested that both $n = 1$ (pure 2D phase) and $n \geq 2$ (quasi-2D phase) can be formed following treatment with a secondary large cation solution, presenting the need for further clarification.^[12,36,37] Crucially, the ambiguity in the low-dimensional phase has led to a number of conflicting reports of the formed heterojunction type and carrier behavior at the interface.^[38,39]

In recent years, some light has been shed on the influence of organic spacer cation choice for the post-treatment of crystallized 3D films.^[40] To date, a number of different organic spacer cations have been incorporated into the perovskite post-treatment solution, including phenethylamine, long-chain alkylammonium halides, polyethylenimine, and trifluoroethylamine.^[6,41–43] Among these works, Seok *et al.* investigated the influence of chain length in alkylammonium spacer cations, finding higher-performing devices and much-improved stability when compared to conventional pure 3D PSCs.^[43] Wang *et al.* compared the passivation effect of electron-donating groups and electron-withdrawing groups based on four phenethylammonium iodide salts.^[44] While further research is still required in producing clearer design criteria for organic cation choice, the effect of the halide anions

is equally essential, yet largely overlooked. As of writing, the impact of halide anion choice on surface passivation has been neglected, and more comparative studies between halide anions are necessitated. The formation of a 2D and/or quasi-2D interlayer has shown to be an effective method to passivate both positive and negative charged point defects.^[45–47] However, to date, the vast majority of 2D/3D perovskite devices have predominantly use iodine-based salts to conduct low-dimensional phase passivation.^[48–52] A transition has recently occurred away from iodide-based spacer cations in favor of bromide-containing salts enabling PSCs among the highest PCEs.^[26,53–55] From this emerging transition, it is clear that the effect of the counter anion in the passivation salts requires detailed further study, considering both crystallographic and optoelectronic properties.

In this work, we seek to offer these much-needed insights into the effect of halide choice on the properties of the low-dimensional perovskite phase. To understand the synergistic role of the halide anions on both quasi-2D layer formation and passivation, we use a post-treatment technique to form low-dimensional structures that present above the $FA_{1-x}MA_xPbI_3$ perovskite on the top surface. To do this, we conduct an in situ secondary growth on the surface of the 3D perovskite film using a series of alkylammonium salt solutions with varying halides, namely neo-pentylammonium iodide (neoPAI), neo-pentylammonium bromide (neoPABr), and neo-pentylammonium chloride (neoPACl). Treating the perovskite films in this way, we next investigate the crucial role of halide anions play in the formation of low-dimensional perovskite structures utilizing state-of-the-art crystallographic techniques. In particular, we identify neoPACl-treated $FA_{1-x}MA_xPbI_3$ as particularly promising for producing high-efficiency devices, owing to an out-of-plane growth of the secondary perovskite phase, enhancing the perovskite crystallinity, and facilitating charge separation. Finally, we conclude our discussion on halide choice by fabricating PSCs and comparing the device properties. The fabricated devices reveal that neoPAX salts considerably enhance the PCEs of the PSCs from 20.93% for the control devices to 22.12%, 22.59%, and 23.35% for the neoPAI, neoPABr, and neoPACl-treated devices, respectively, while also improving long-term stability. Our work thus provides a novel and thorough perspective into the formation mechanism of low-dimensional interlayers with multi- n values induced by different halide substitutions via in situ secondary growth.

2. Results and Discussion

In this work, 3D perovskite films based on a double-cation composition of $FA_{1-x}MA_xPbI_3$ ((FAMA)PbI₃) were fabricated using a sequential two-step deposition process, with MACl as an additive (experimental details provided in the Supporting Information).^[20] For the secondary growth of the low-dimensional phase, neoPAX salts were deposited following a conventional procedure,^[43] spin-coating a 25 mM neoPAX isopropanol solution onto the 3D perovskite surface before annealing. The resulting changes in the morphology of the perovskite film following the neoPAX deposition were characterized using a combination of scanning electron microscopy (SEM) and atomic force microscopy (AFM). In the unmodified control films, the perovskite exhibits large grains with an average grain size of $\sim 1 \mu m$ and a thickness of 650 nm (Figure 1a,c). Additionally, we observe small plate-like features on the film surface with a bright contrast, attributed to PbI₂ at the GBs. Upon the addition of the neoPAX solution, a distinct change in surface morphology is observed. Regardless of the halide choice, the perovskite surface

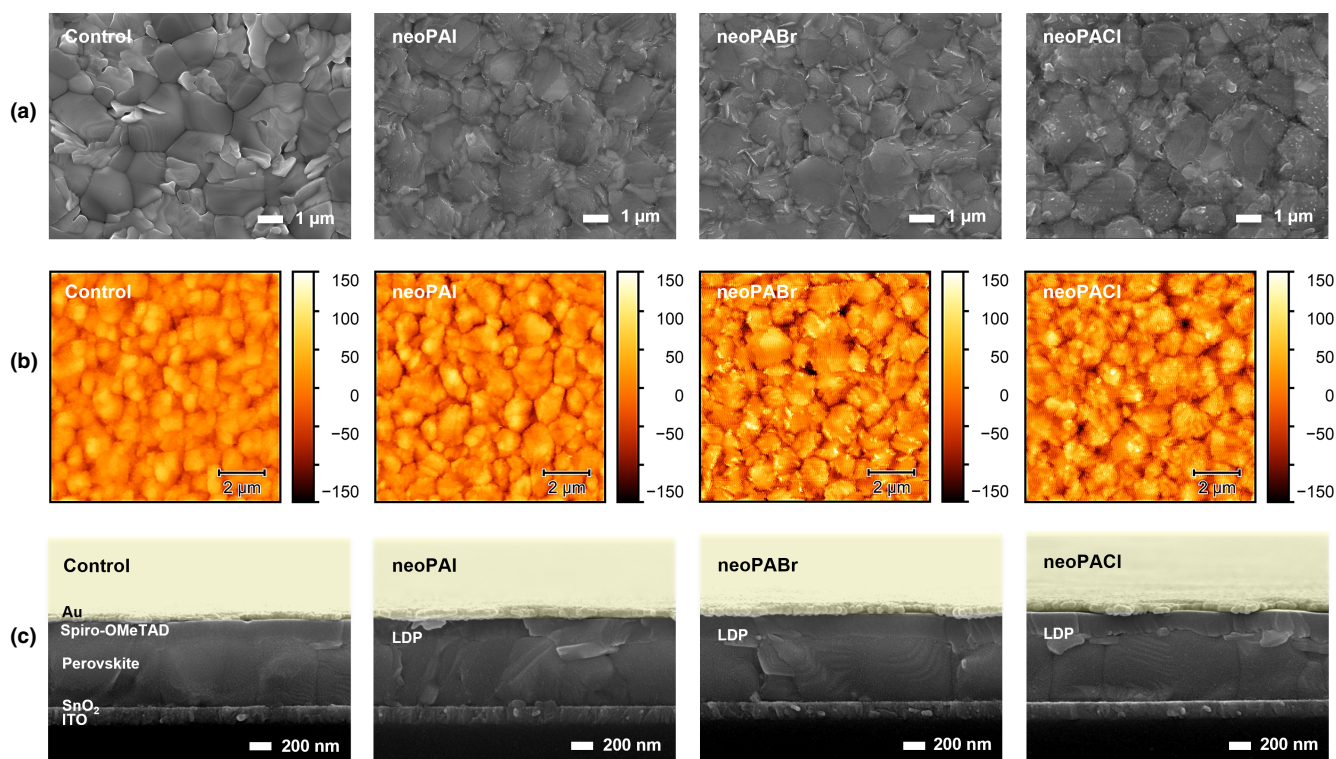


Figure 1. a) Surface morphologies of perovskite films without and with LDP-optimized treatment conditions acquired with scanning electron microscopy. b) Atomic force microscopy images of control and LDP-passivated perovskite films. c) Cross-sectional SEM images of the control and LDP-passivated perovskite films with contact layers.

morphology is changed, forming new flake-like features. The newly formed flake-like structures on the perovskite surface are consistent with previous reports of phase changes occurring at the surface from 3D to low-dimensional phases and indicate a secondary nucleation step has occurred.^[56,57] The change in surface morphology is further observed in AFM topography measurements of the neoPAX-treated films (Figure 1b and Figure S1). Accordingly, the calculated root-mean-square roughness (R_{RMS}) of the various LDP modified films (Figure S2) are larger than the control value of 31.34 ± 8.79 nm, reaching 42.37 ± 9.42 , 44.67 ± 5.23 , 45.34 ± 7.47 nm for I, Br, and Cl halide salts, respectively. The increased roughness relative to the control is attributed to the formation and nucleation of a new perovskite phase on the surface combined with recycling and removal of material from the perovskite substrate needed to form the new phase.^[56]

To further understand how the crystallography of the new phases observed in the surface microscopy varies between the halides, crystallographic measurements were conducted using surface-sensitive grazing incidence wide-angle X-ray scattering (GIWAXS). Comparing the diffraction patterns in Figure 2a–d (scattering intensity maps in reciprocal length units), the neat pseudo-cubic FA(MA)PbI₃ perovskite exhibits two primary grain orientations, with crystallinity predominantly in the out-of-plane direction (peaks observed at $[100]_c$ ($q = 1 \text{ \AA}^{-1}$) and $[200]_c$ ($q = 2 \text{ \AA}^{-1}$) in Figure 2a) as analyzed the perovskite (100) azimuthal intensity profile in Figure S3.^[19] Upon conducting the neoPAX treatment, the texturing of the diffraction rings is slightly enhanced, confirming a recrystallization process occurs during the in situ secondary reactions, improving the film crystallinity (Figure 2a–d, i). Azimuthally integrated 1D scattering in Figure 2e shows characteristic

reflections from the pseudo-cubic FA(MA)PbI₃ perovskite, as well as PbI₂ in all samples at 0.91 \AA^{-1} (equivalent $\text{Cu K}\alpha$ $2\theta = 12.8^\circ$). Significantly, the intensity of the PbI₂ signal intensity is reduced in the neoPABr- and neoPACl-treated samples. These reductions in PbI₂ intensity are observed concurrently with the emergence of a scattering feature at 0.48 \AA^{-1} (6.8°) in treated samples, linked to the low-dimensional phase formation. From this low grazing angle (1°) observation, it is concluded that the excess PbI₂ phase on the surface of the pristine perovskite film is partially consumed in order to form a low-dimensional phase at the surface region. We therefore identify that PbI₂ on the surface is predominantly the Pb²⁺ source for the formation of low-dimensional phases when using neoPABr and neoPACl, rather than the 3D perovskite, as discussed in further detail in later sections. This observation of PbI₂ consumption is further encouraged by the removal of the bright contrast flake structures in the SEM images of treated films, which is attributed to the PbI₂. Such consumption of residual PbI₂ to form 2D phases is consistent with previous works in which phenethylammonium iodide is deposited on 3D perovskite.^[25,58] Interestingly, different behavior is observed in the case of iodide-based salts, suggesting the formation of low-dimensional phases is dependent on the halide choice in the passivating salts, discussed in greater detail in further sections.

While the neoPA⁺ cation has not yet been reported to form Ruddlesden–Popper phases, it is similar in length and structure to other branched alkylammonium cations such as isobutylammonium (isoBA) but with an additional branched methyl group (Figure S4). As with other alkylammonium cations,^[59] the isoBA cation has been reported to form layered structures with the general composition

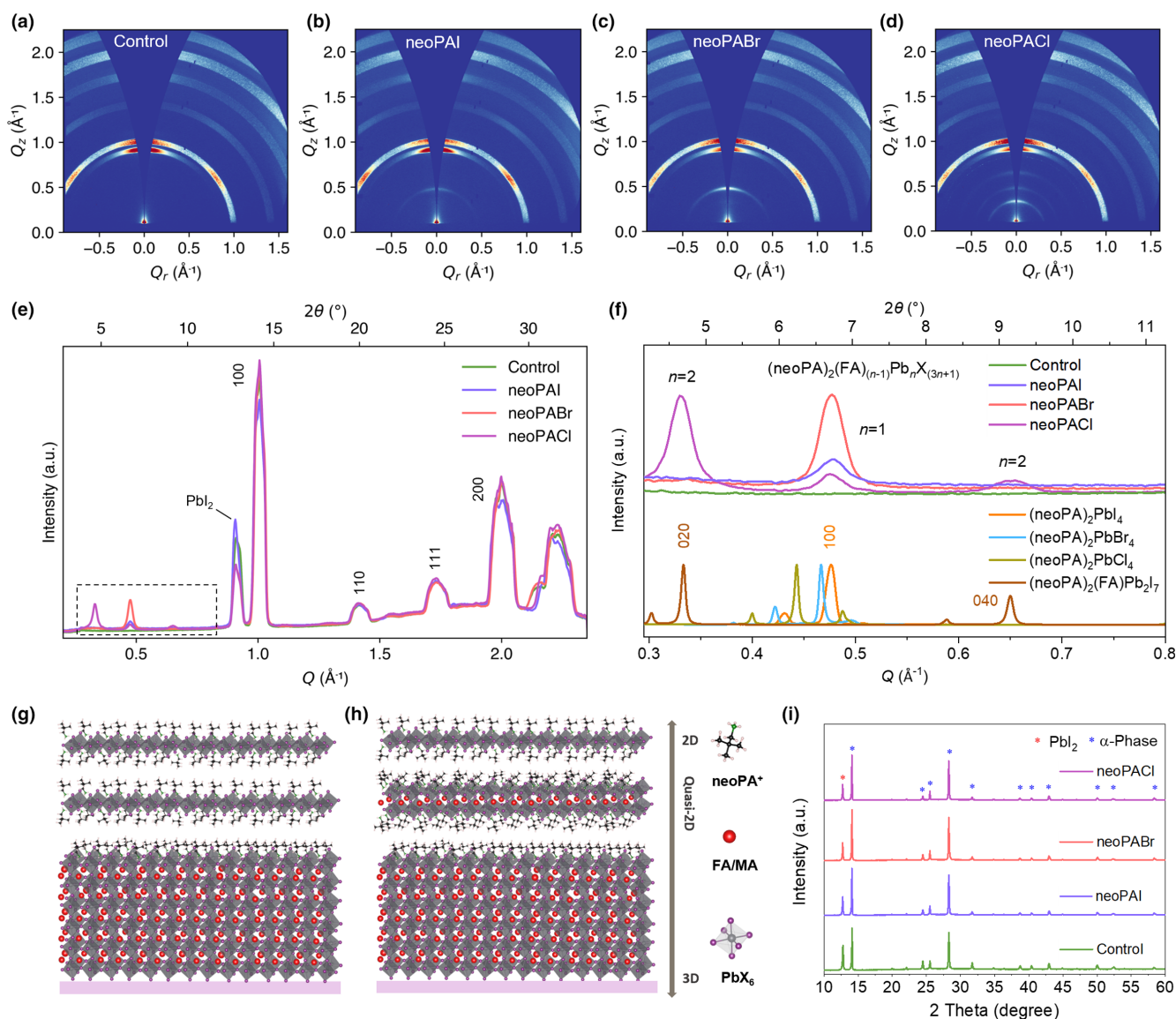


Figure 2. GIWAXS characterization of microscopic crystal structure of neat and neoPAX-treated FA(MA)PbI₃ films. a–d) 2D scattering of neat and LDP-passivated perovskite films by neoPAI, neoPABr, and neoPACl at a grazing angle of $\alpha_i = 1^\circ$. e) Azimuthally integrated scattering for neat perovskite film and LDP treatment films with Miller indices of reflections from the perovskite phase marked, collected at an incidence angle $\alpha_i = 2^\circ$ to minimize peak broadening. f) The highlighted low-angle region with marked reflections ascribed to newly formed $(\text{neoPA})_2(\text{FA})(\text{MA})_{n-1}\text{Pb}_n\text{X}_{(3n+1)}$ Ruddlesden–Popper phases. These are compared to normalized X-ray diffraction patterns from neo-pentylammonium lead halide thin films. g, h) Schematic structures of 2D/3D and quasi-2D/3D perovskite films induced by neoPAX with different anions. i) XRD patterns of perovskite films without and with neoPAX incorporation.

$(\text{isoBA})_2(\text{MA})_{n-1}\text{Pb}_n\text{X}_{(3n+1)}$ where X is a halide anion.^[60–63] Of these layered structures, two $n = 1$ phases have been directly synthesized, namely $(\text{isoBA})_2\text{PbI}_4$ (Figure S5) and $(\text{isoBA})_2\text{PbBr}_4$, which occupy monoclinic structures with distorted octahedral layers at room temperature (space group $P2_1/c$).^[60,62] The $n = 2$ $(\text{isoBA})_2(\text{MA})\text{Pb}_2\text{I}_7$ composition expresses a slightly monoclinic structure with greatly reduced octahedral distortions,^[62] a trend which continues with the higher $n = 3, 4$ members (all indexed with space group $C2/c$).^[63,64] In these films, because of the similar chemical characteristics of the isoBA^+ and neoPA^+ cations, we expect comparable structures will be adopted if they are formed during the post-treatment, resulting in phases with composition $(\text{neoPA})_2(\text{FA})(\text{MA})_{n-1}\text{Pb}_n\text{X}_{(3n+1)}$.

Scattering patterns of the films at different incidence angles between 0.2° and 1.0° were collected to further explore the phase changes from the surface to the bulk perovskite (Figure S6).^[65,66] Reducing the incidence angle of the X-rays (0.2°) to shorten the probe depth in the perovskite film and increase surface sensitivity, we found that low-dimensional scattering features are present at higher intensity relative to the 3D perovskite substrate at the surface. As expected from the evidence of secondary growth on the surface imaging, this result emphasizes that the new low-dimensional phases tend to be distributed at the top surface of the 3D perovskite substrate. In all cases, we find that the addition of a large spacer cation (neoPA^+) forms new scattering features which are orientated out of plane and have larger d-spacings

than the pristine perovskite, the $n = 1$ (100) and $n = 2$ (020) azimuthal intensity profile have shown in Figure S7. The patterns are thus indicative of forming a quasi-2D/3D heterojunction structure with parallel orientation and layered phases. We next consider the more subtle differences between the different crystallography of the halides.

To probe the direct influence of different halide anions on crystallographic properties, we first compare the scattering features from the quasi-2D phases using grazing incidence X-ray diffraction (GIXRD), with the characteristic peaks of neoPAX powders (Figure S8). Using this approach, we confirm that the new phases formed are indeed low-dimensional perovskite materials rather than the crystallized neoPAX powder on the surface. We next fabricated low-dimensional $(\text{neoPA})_2(\text{FA})_{(n-1)}\text{Pb}_n\text{X}_{(3n+1)}$ thin films with structures of $n = 1$ $(\text{neoPA})_2\text{PbI}_4$ and $n = 2$ $(\text{neoPA})_2\text{FAPb}_2\text{I}_7$ to act as references. The resultant diffraction patterns were compared with the X-ray scattering patterns from these films with the peaks from treated samples, as shown in Figure 2f. The thin film measurements confirm that the peak at $q = 0.48 \text{ \AA}^{-1}$ is from the $n = 1$ LDP phase and is attributed to the (100) reflection of the $(\text{neoPA})_2\text{PbI}_4$ 2D perovskite. In a key observation, we find that the $n = 1$ (100) reflection of $(\text{neoPA})_2\text{PbI}_4$ at 0.48 \AA^{-1} was present in all neoPA⁺-treated samples regardless of halide choice (Figure 2f). This suggests that the iodide-based low-dimensional phase is the thermodynamically favorable composition, and thus, the neoPA⁺ reacts with iodide from PbI_2 preferentially rather than the halide of the salt (Br^- , Cl^-), to form a low formation energy iodide phase.^[60,67,68] We attribute the iodide-based phase formation to the preferential reaction between neoPA⁺ and excess PbI_2 on the pristine 3D perovskite film, instead of reacting with native anions (Br^- or Cl^-) introduced from the neoPAX salts. This is in good agreement with the previously discussed reduction in PbI_2 intensity in GIWAXS. In the case of using neoPAI, the halide required to form the iodide-based perovskite phases is the native salt halide, and as such, the formation is likely modified. This is reflected in the larger PbI_2 and smaller [100] 3D-phase reflections when perovskite films are treated with neoPAI, attributed to localized break down of 3D perovskite at the film surface.

To further confirm our finding that solely iodide phases are formed, we fabricated low-dimensional perovskite films consisting of pure $(\text{neoPA})_2\text{PbBr}_4$ and $(\text{neoPA})_2\text{PbCl}_4$ for comparison with neoPAX-treated samples (Figure 2f and Figure S9A). Comparing the (100) peak positions, we observe that the $(\text{neoPA})_2\text{PbBr}_4$ and $(\text{neoPA})_2\text{PbCl}_4$ phases have a greater interlayer spacing in the (100) plane than $(\text{neoPA})_2\text{PbI}_4$ and subsequently exhibit diffraction peaks at lower angles in the X-ray diffraction (XRD) patterns (Figure 2f). This is consistent with the reference X-ray scattering patterns from three isobutylammonium lead halide phases with the peaks in our data (Figure S10). Consistent with our findings, we note that no shift of the (100) peak at 0.48 \AA^{-1} (6.8°) is observed in all three treated films, further proving the $n = 1$ low-dimensional perovskite component is $(\text{neoPA})_2\text{PbI}_4$.

In the previous section, we have discussed the tendency of all halides to form pure iodide-based low-dimensional phases. However, it is notable that differences remain in terms of the n number. As discussed, GIWAXS patterns of the treated perovskite surface reveal that both neoPAI- and neoPABr-treated samples exhibit a clear $n = 1$ corresponding to $(\text{neoPA})_2\text{PbI}_4$ (Figure 2f,g), with stronger low-dimensional peaks in neoPABr sample; thus, in turn it corresponds to the difference in surface morphology (Figure 1a). Interestingly, in the case of the neoPACl, extra phases can also be distinguished from the diffraction pattern. The features are indexed as reflections from $(\text{neoPA})_2\text{FAPb}_2\text{I}_7$, with the (020) peak at $q = 0.33 \text{ \AA}^{-1}$ (4.6°) and (040) at $q = 0.65 \text{ \AA}^{-1}$ (9.1°)

(Figure 2f,h). Partial Bragg rings are observed (Figure 2d) with the highest intensity along the q_z axis, which can be ascribed to the quasi-2D perovskite forming with a slight texture, in agreement with the discussed morphological characterization.^[52,69,70] Additionally, we also confirm no detectably large scattering domains of higher n -value quasi-2D phases present even when neoPAI and neoPABr concentrations increase to 50 mM (Figure S9B), which excludes the effect of halide concentration on the formation of quasi-2D phases.

Taken together with these results, we find that the halide anion strongly influences the recrystallization dynamics and the degree of dimensionality (n value) of the secondary low-dimensional phases rather than the composition. The tendency to form $n > 1$ phases after chloride-salt incorporation could result from the preferential coordination of halogen due to the electronegativity between the metal ions and different halide anions,^[71] resulting in multiple $[\text{PbI}_6]^{4-}$ octahedral units and a thicker layered structure. Despite noting the formation of the new iodide-based low-dimensional phases in the neoPACl-treated samples, it remains unclear if the Cl^- is partially incorporated into the bulk perovskite composition, or plays a role in the crystal growth, similar to MACl during the recrystallization process.^[27,63]

To gain a better understanding where the native halide anions from the added salts are distributed within the modified perovskites, time-of-flight secondary-ion mass spectroscopy (ToF-SIMS) was performed with both negative and positive polarity (Figure 3a–d). As expected, neoPA⁺ cations were observed with higher intensity at shorter sputtering times, which further confirms that 2D and quasi-2D perovskite phases are present at the perovskite top surface rather than being uniformly distributed throughout the bulk perovskite films (Figure 2g,h), consistent with the previous GIWAXS conclusions. While it is not possible to distinguish I^- and Cl^- anions introduced by the neoPAX salt in the 3D perovskite films which contain native I^- and Cl^- anions, we speculate that the additive halides become distributed in a similar fashion to that of the Br^- distribution. Significantly, we observe that the introduced Br^- anions exist throughout the bulk perovskite film when films are treated with neoPABr. This conclusion is supported by Cl^- being present in a similar profile to that of Br^- in the neoPACl-treated sample, suggesting that the introduced Cl^- also diffuses within the film (Figure 3e). Furthermore, we note no significant change between the neoPAI-treated film and control in the iodide distribution; this is attributed to the additional iodide forming 2D interlayer. This phenomenon suggests that the small halide ions readily migrate and diffuse through the perovskite during the post-treatment process.^[72,73] Previous works have shown that diffusion of Br and Cl halides into the bulk of the perovskite from a surface treatment can have a profound passivation effect, particularly on deep-trap states.^[73] We expect similar passivation of trap states to occur from the diffusion of the neoPAX halide within the bulk, as discussed more detail in the following sections.

To probe the effect of the diffused additive halides on point defects within the perovskite film, we investigate the change in micro-strain of the 3D perovskite film. It has been reported that residual lattice micro-strain in perovskites is directly associated with reduced point defect concentrations and thus lower nonradiative recombination.^[74,75] Williamson–Hall (WH) plots (Figure S11) were employed to estimate the variation in lattice strain (ϵ) of LDP-terminated films from the XRD patterns using multiple peaks from the 3D perovskite phase, calculated in Figure 2i. As shown in Figure 3f, for the LDP-passivated perovskite surface, the micro-strain in these quasi-2D/3D perovskite films is dramatically decreased, showing a trend of $\epsilon_{(\text{control})} > \epsilon_{(\text{neoPAI})} > \epsilon_{(\text{neoPABr})} > \epsilon_{(\text{neoPACl})}$. The lowest strain occurs

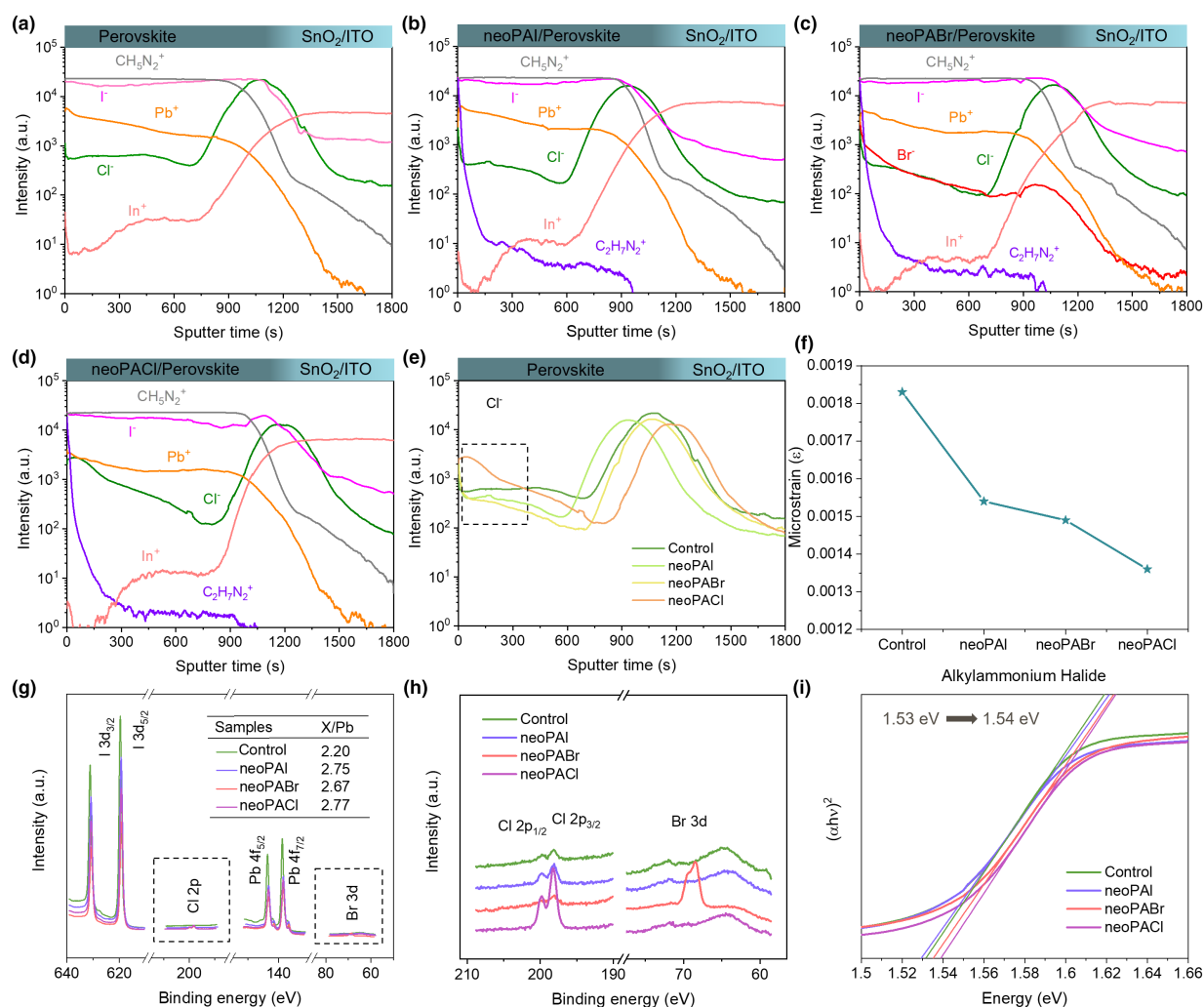


Figure 3. a–d) ToF–SIMS depth profile analysis of pristine perovskite, neoPAI-, neoPABr- and neoPACl-treated perovskite samples. e) Comparison of Cl⁻ anions between different treated samples and pristine perovskite films. f) Residual strain calculated in various perovskites consisting of glass/perovskite. g) The high-resolution I 3d, Cl 2p, Br 3d, and Pb 4f core energy level spectra and X/Pb (X=I, Br, Cl) ratio from various perovskite films. h) High-resolution Br 3d and Cl 2p core-level spectra of perovskite films without and with the passivation of neoPAX. i) Tauc plots of the perovskite thin films prepared without and with neoPAX post-treatment.

when neoPACl is incorporated onto the FA(MA)PbI₃ surface. This observation is consistent with the diffusion of bromide and chloride ions into the perovskite film, leading to the passivation of point defects and a reduction in strain. Therefore, we identify that the choice of halide salts in post-treatment processing has a significant effect on reducing residual lattice micro-strain and defect states, further improving the overall crystallinity of the perovskite film.

To further probe the changes in the 3D perovskite film, a full XPS spectrum for the various passivated perovskites was carried out, revealing the elemental distribution, as shown in Figure S12A. For the N 1s spectrum in all samples, the feature around 400.6 eV can be attributed to the C=N bond in the FA⁺ cation (Figure S12B).^[44] The characteristic C=N peak moves to lower binding energies with the incorporation of the LDPs, which is likely a consequence of the electron-donor effect from neoPA⁺ cations, forming a more electron-rich environment around the FA⁺.^[76] We note that an extra C–N peak emerged after

LDP passivation at a binding energy of 402.2 eV that we assign to be the C–N bond in neoPA⁺. Furthermore, we examined the average halide/lead (X/Pb) ratio at a depth of around 10 nm of the film surfaces to semi-quantitatively analyze the various perovskite interfaces (Figure 3g). From high-resolution I 3d, Br 3d and Cl 2p core-level spectra (Figure 3h and Figure S12C), the X/Pb ratio is calculated as 2.20 for the pristine film, while values 2.75, 2.67, and 2.77 were recorded for neoPAI, neoPABr, and neoPACl-passivated samples, respectively. This increase may derive from the extra added halide anions and a minor reduction of PbX₂ at the interface. In turn, we speculate this effect helps to reduce the halide vacancies on the perovskite film surface and inside the bulk, removing traps and improving the transport and extraction of carriers at the heterojunction interface.^[77] Conducting UV–visible (UV–vis) spectroscopy revealed a blue shift of absorption edge after the LDP formation induced by neoPABr or neoPACl compared to the control sample (Figure S12D). This effect is most notable

in the neoPACl-passivated sample, where Tauc plots constructed of the absorption onset reveal a slightly enlarged optical bandgap from 1.53 to 1.54 eV (Figure 3i). This shift of the band edge further demonstrates that the Cl and Br diffuse into the 3D phase and altering the composition, in agreement with our previous discussion.

We further studied the photophysical properties of the neoPAX-treated perovskite films compared to the pristine film. To discern the origin of the blue shift, steady-state photoluminescence (PL) was conducted on both sides of the films. Measuring the rear surface of the neoPAX-treated samples, we see a clear blue shift going increasing from $\text{Cl}^- > \text{Br}^- > \text{I}^-$ (Figure 4a). The observed blue shift indicates that the choice of halide has a clear influence on the bulk perovskite through the film, owing to anion exchange and diffusion as previously discussed in the ToF-SIMS and UV-vis measurements.^[46] After LDP passivation, the PL spectrum also exhibits increased intensity, while the absorbance in the UV-vis and film thickness remain approximately constant. This result further suggests that the defect concentration is reduced, suppressing the nonradiative recombination of carriers.^[78] Interestingly, PL conducted with front excitation shows three emission peaks at higher energy (Figure 4b), which can be attributed to the emission from the LDP phases with $n = 1, 2$ and 3. The appearance of a peak around 600 nm in the PL spectra upon front excitation at a shallow angle (20°) suggests that small regions of $n = 3$ may exist within the low-dimensional phases and can be observed using highly sensitive, high fluence, and steady-state optical spectroscopic techniques. This result is consistent with the existence of multi- n values in the 2D/3D structure in previous works.^[79–81]

In addition to steady-state PL, time-correlated single photon counting (TCSPC) was carried out to probe the charge-carrier decay

dynamics and gain insights into nonradiative carrier recombination processes in the LDP-passivated films (Figure 4c). The PL decay curves were measured using the peak emission at 800 nm, and the average carrier lifetime values were fitted with the bi-exponential equation $Y = A_1 \exp(-\tau/\tau_1) + A_2 \exp(-\tau/\tau_2)$.^[82] The longer average lifetimes in the LDP-passivated films highlight that the modified perovskite film undergoes a slower depletion of the photogenerated carriers, attributed to the passivation effects of the quasi-2D phase on the 3D perovskite phase, when measuring from the passivated side, thus reducing the nonradiative recombination which occurs at the interface (Table S1). Within these quasi-2D/3D films, the low-dimensional interlayer with an additional $n = 2$ phase induced by using neoPACl significantly enhances the film quality and carrier lifetime from 110 ± 0.01 ns of the control film to 692 ± 0.01 ns.

To better evaluate the LDP-based perovskite carrier transport properties, the trap density of electrons and holes were evaluated quantitatively by space-charge limited current (SCLC) measurements. Electron-only devices with the structure of ITO/SnO₂/perovskite/PCBM/Au and hole-only devices with ITO/perovskite/Spiro-OMeTAD/Au were fabricated (see Experimental Section in Supporting Information). Figure 4d,e show the dark current-voltage curves with an ohmic region, a trap-filled limited (TFL) region, and a trap-free SCLC region. The trap density (N_t) was calculated as previously reported,^[83,84] using the trap-filled limit voltage (V_{TFL}) from the equation of $N_t = 2\varepsilon_0\varepsilon_r V_{\text{TFL}}/qL^2$, where ε_0 is the vacuum permittivity, ε_r is the relative dielectric constant,^[85] q is the elementary charge, and L is the thickness of the perovskite films. V_{TFL} is then obtained by fitting the dark current-voltage curves. It is found that after modification of perovskite with neoPACl, the electron defect density of perovskite film is

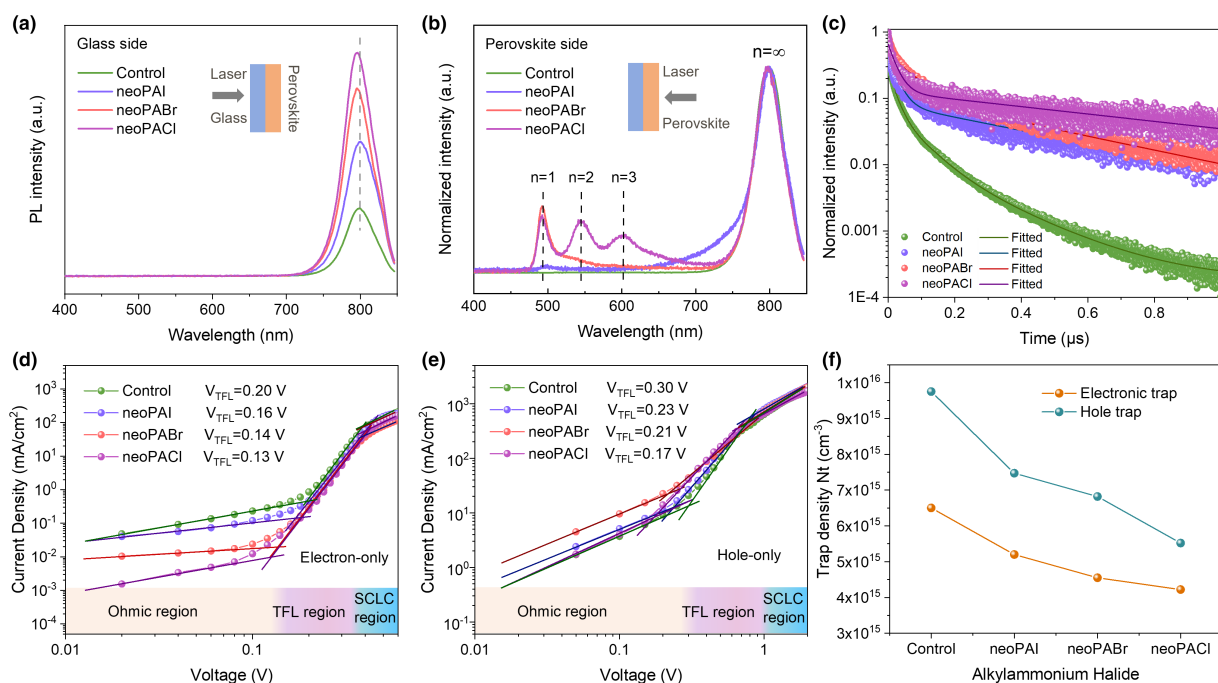


Figure 4. a, b) Steady-state photoluminescence spectra of quasi-2D layered perovskite formed after neoPAX treatment measure from the backside (glass side) and front side (perovskite side). c) Time-resolved photoluminescence kinetics for the pristine and LDP-passivated perovskite films. d, e) Dark current-voltage measurements of the electron-only devices and hole-only devices passivated by neoPAX. f) Calculated electron trap density and hole trap density.

reduced from 6.50×10^{15} to $4.22 \times 10^{15} \text{ cm}^{-3}$, and the hole defect density decreased from 9.75×10^{15} to $5.52 \times 10^{15} \text{ cm}^{-3}$ (Figure 4f). This observation is consistent with the reduction in lattice micro-strain and could be attributed to a combination of highly oriented and crystalline films when using the LDP interlayer, and the passivating effect of diffused halides introduced from the neoPAX treatment.^[73]

In the previous discussion, we find that using neoPACl exhibits the most benefit to the crystallographic and optoelectronic properties. To further characterize the carrier dynamics in quasi-2D/3D heterojunction induced by neoPACl, transient reflection (TR) spectroscopy measurements were carried out.^[86] Figure 5a shows the TR spectra of the neoPACl-passivated perovskite active layer with a thickness of $\sim 650 \text{ nm}$ under a 520-nm pump from the front side. Two sharp negative features positioned at 540 and 790 nm are observed, indicating a photoexcitation of two distinct energy levels. Previous work has shown that for thick perovskite crystals, where a relatively large refractive index applies, the inverse Hilbert transform of the TR spectrum is approximately proportional to the transient absorption (TA) spectrum.^[87] Under an inverse Hilbert transform shown in Figure S13, the low-energy sharp feature in the TR spectra indicates a ground state bleach peaking at $\sim 790 \text{ nm}$ in the “pseudo-TA” spectra, corresponding to the band edge of the 3D FA(MA)PbI₃ perovskites. This is further confirmed by the TR spectra of a pristine 3D FA(MA)PbI₃ perovskite in Figure 5d, where identical low-energy features are observed. To identify the nature of the high-energy feature, a low-photon-energy pump (720 nm) was used to excite the neoPACl-passivated perovskite sample from the front side as shown in Figure 5b. Under these excitation conditions,

only the low-energy feature can be observed, consistent with the spectra observed for pure 3D perovskites under the same excitation conditions (Figure 5e). This observation rules out the possibility of a higher-lying sub-band structure at 540 nm introduced by neoPACl. As a result, we attribute the high-energy transient feature in Figure 5a to the quasi-2D species with $n = 2$, as confirmed by GIWAXS and XRD in Figure 2.

Figure 5c shows the normalized kinetics of the quasi-2D and the 3D species for neoPACl-treated sample (see non-normalized data in Figure S14). A sharp decrease in the 540-nm feature is accompanied by an initial (around $\sim 1 \text{ ps}$) increase in the 760-nm feature. This indicates an efficient charge transfer from the quasi-2D species to the 3D species at the interfaces (see the kinetics of pristine 3D perovskites in Figure S15). After this process, the 540-nm feature decays completely within $\sim 1 \text{ ns}$, due to the repopulation of the ground state of the quasi-2D species. This time scale and the spectral energy match the radiative recombination processes of excitons in the $n = 2$ component detected by TCSPC at 580 nm (Figure S14C). Figure 5f shows a diagram of carrier dynamics in neoPACl-passivated perovskite structures. The energy levels of quasi-2D perovskite induced by neoPACl were estimated from ultraviolet photoelectron spectroscopy (UPS).^[25] The Fermi level and valence band minimum for neoPACl-passivated perovskite film are calculated to be -3.97 and -5.77 eV , respectively (Figure S16). Under a 520-nm pump, photoexcitations are promoted inside the quasi-2D species at the front surface of the sample, leading to the depopulation of the ground state of the $n = 2$ species. The photoexcitations near the quasi-2D/3D interfaces undergo ultrafast charge transfer ($\sim 1 \text{ ps}$) into the 3D perovskite, and the excitons inside the quasi-2D perovskite that

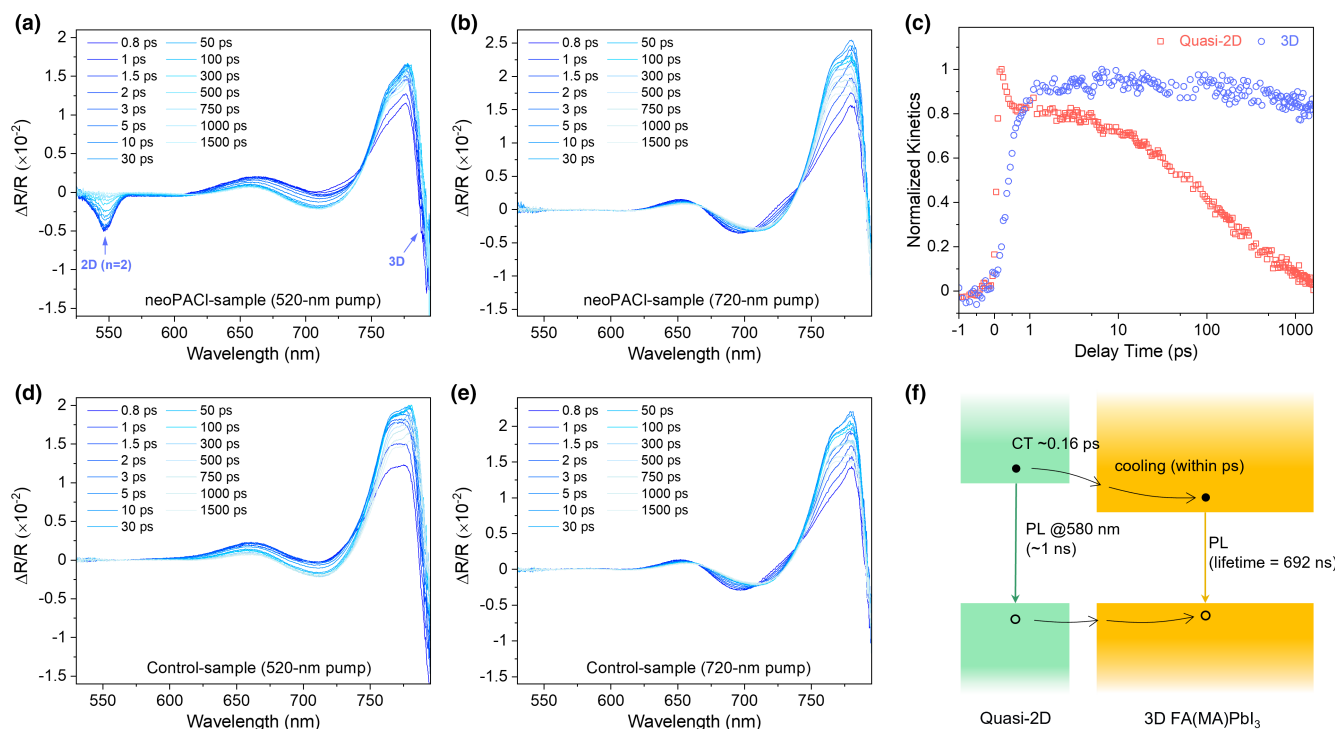


Figure 5. Carrier dynamics analysis in quasi-2D/3D perovskite films. a, b) Transient reflection (TR) spectra of a neoPACl-passivated sample under a 520-nm pump and a 720-nm pump. c) Normalized kinetics (-1 to 1500 ps) of band-edge carriers of quasi-2D ($n = 2$) and 3D components of a neoPACl-passivated sample under a 520-nm pump. d, e) TR spectra of a pure 3D FA(MA)PbI₃ perovskite sample on a glass substrate under a 520-nm pump and a 720-nm pump. f) Schematic illustration of photoexcitation dynamics for the neoPACl-passivated sample under a 520-nm pump.

are spatially separated from the 3D perovskite undergo recombination processes with a lifetime of ~ 1 ns. The charge carriers inside the 3D components are initially “hot” carriers with carrier temperatures higher than the lattice temperature.^[88] These hot carriers undergo efficient carrier-phonon interactions and cool down to the conduction band edge of the 3D perovskite within ~ 2 ps.^[89] TCSPC shows a photoluminescence lifetime of ~ 692 ns in neoPACl-passivated samples, longer than the lifetime in pristine samples of ~ 110 ns. (Figure 4c). This further indicates the energy transfer could be facilitated by the quasi-2D perovskite interlayer, and the closely separated energy levels of the quasi-2D/3D heterojunction may lead to a more efficient energy transfer route in comparison with the pristine 3D perovskite film. The location of the quasi-2D ($n = 2$) perovskite above the 3D components at the front surface is further confirmed by exciting the samples under a 520-nm pump from the back (Figure S17), where similar spectra are observed for a neoPACl-passivated sample and a control sample, indicating negligible amounts of quasi-2D ($n = 2$) perovskite phase at the back. Based on these results, we conclude that the presence of a quasi-2D perovskite with $n = 2$ on the 3D perovskites extends the carrier lifetime significantly and can spatially separate carriers. Such removal of electrons away from the perovskite/HTL interface induced by neoPACl is ideal behavior for minimizing recombination at the interfaces in high-performing PSC devices.

Finally, we fabricated PSCs with an ITO/SnO₂/perovskite/Spiro-OMeTAD/Au architecture to understand how the photovoltaic performance of the PV devices employed varies with the choice of organic spacer halide. Firstly, we optimized the concentration of the secondary growth solution to form quasi-2D structures, exploring the effect of concentration on device performance (Table S2). The devices achieved optimal PCEs upon incorporating 25 mM of neoPAX/IPA solution. **Figure 6a** shows the current density-voltage ($J-V$) characteristics of champion devices with the post-treatment passivation strategy. Compared with the devices without LDP treatment, the V_{oc} is significantly enhanced from 1.09 to 1.16 V after neoPACl passivation, demonstrating the excellent suitability of LDP modifier layers to passivate trap defects at the perovskite surfaces and bulk, while enhancing the quasi-Fermi level splitting. The control devices based on pristine FA(MA)PbI₃ show a maximum PCE of 20.92%, with a large hysteresis, which points to a defect-rich perovskite film. In comparison, the PV devices passivated by neoPACl exhibit a champion PCE up to 23.35%, a significantly enhanced V_{oc} of 1.16 V, a J_{sc} of 24.71 mA cm^{-2} , and an FF of 81.62% (Figures S18 and S19). The negligible hysteresis further proves that the defect-rich interface is passivated by the post-treatment. The increased J_{sc} and FF demonstrate that in all cases, efficient carrier transport occurs. External quantum efficiency (EQE) spectra of the devices are also compared in Figure 6b. An integrated J_{sc} of 24.57 mA cm^{-2} from the neoPACl-treated device is well matched with the value obtained from the $J-V$ curves ($<1\%$ discrepancy), whereas the control device showed an integrated J_{sc} of 24.07 mA cm^{-2} . The enhanced performance could be attributed to the improved perovskite film quality, reduced trap density and efficient electron-blocking by the quasi-2D perovskite layer at the 3D perovskite/hole transport layer (HTL) interface, which stands out among similar 2D/3D structured devices (Table S3). Figure 6c shows the steady-state PCE measured at the maximum power point (MPP) of the PSCs. A stabilized PCE of 23.07% was obtained for the device passivated with neoPACl biased at 1.00 V, whereas that of the control device is 20.27% at 0.92 V.

We finally consider the choice of halide on stability, contact angle measurements were conducted to investigate any changes in

hydrophobicity of the perovskite surface with varying halides. Imaging the instantaneous contact angle of a water droplet upon contact with various neoPAX-treated perovskite films revealed a reduction in hygroscopicity compared to the pristine perovskite film, which is a consequence of the hydrophobic quasi-2D perovskite barrier layer (Figure 6d). The quasi-2D terminated interface shows an excellent ability to block water vapor erosion, especially in the neoPACl-treated sample. We note that improved hydrophobicity could also originate from the more slightly rougher film, increasing the amount of contact between the hydrophobic surface and water droplet. The improved moisture stability is further supported by high-resolution XPS measurement, the C=O peak (~ 288.2 eV), related to the reaction between organic component and oxygen/water exposure on the surface of perovskite film,^[90,91] was significantly suppressed in the LDP-terminated perovskite film (Figure 6e). This shows that surface treatment with neoPAX can effectively protect the perovskite from oxygen and moisture in an ambient environment. Moreover, we find that the passivated perovskite films maintain stable α -phases after 300 h of storage in the atmosphere (20%RH) from Figure S20, while the PbI₂ peak in the pristine sample increases significantly, a result of environmental moisture washing out A-site cations and leaving PbI₂. As a result, the unencapsulated devices fabricated via the neoPACl passivation strategy exhibit significantly improved stability when stored under dark and ambient conditions with a relative humidity of 20%. These dark storage studies estimate the shelf life of PSCs under environmental conditions without exposure to light, which in line with the ISOS D-1 stability test.^[92] The control device retained around 80% of its initial efficiency after 15:00 h of storage. In contrast, the neoPACl-passivated device maintained $>95\%$ of its initial PCE (Figure 6f and Figure S21), demonstrating an increased environmental resistance compared with the use of bromide and iodide salts. Improved long-term stability is attributed to better interfacial contact between the quasi-2D/3D interface and the HTL. This is crucial for facilitating efficient hole transfer at the interface and helping achieve long-term device stability.^[49]

3. Conclusion

In summary, we highlighted the importance of halide choice in large organic spacer salts for quasi-2D/3D heterojunction engineering. In doing so, we investigated a new organic cation with three different halides, neoPAX ($X = \text{I}, \text{Br}$ or Cl). After systematically comparing and analyzing the effect of halide choice on formation mechanism, crystallography, and the photoelectric properties of quasi-2D/3D heterojunctions, we identify that neoPACl exhibits the optimum benefit to devices. In a key insight into the formation mechanism of the secondary low-dimensional phases, we observe that the newly formed perovskite phases are iodide-based in nature regardless of the halide used in the salts. However, while neoPABr and neoPAI produce a pure 2D perovskite film, neoPACl promotes the formation of quasi-2D perovskites with multiple phases ($n = 2$) induced by the strong electronegativity of the Cl^- . ToF-SIMS characterization identified the distribution of Cl^- and Br^- ions introduced from the passivation treatment but not incorporated into new perovskite phases, revealing diffusion into the 3D perovskite. Constructing Williamson–Hall plots of the 3D perovskite crystallographic properties, we see a decrease in lattice micro-strain, indicating that the diffused non-native halides passivate and improve the crystallinity of the bulk. Conducting ultrafast ps TAS on the optimum neoPACl-treated sample, we identify beneficial carrier

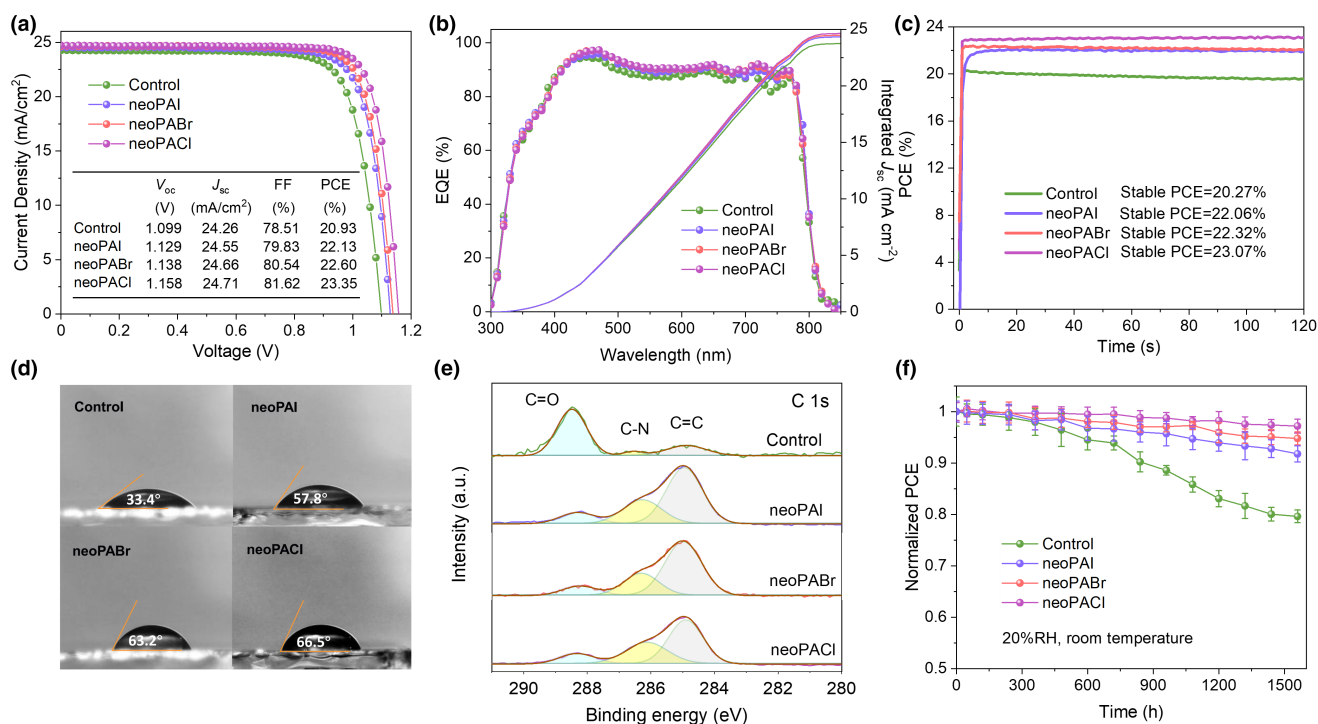


Figure 6. a) J - V curves with reverse (1.2 to -0.1 V) scans of devices fabricated with the untreated film and with different alkylammonium halide treatment. The scan rate is 100 mV s^{-1} . b) EQE curves and integrated current density spectra of control and post-treatment devices. c) Stabilized PCEs measured under maximum power point tracking for 120 s of various devices (voltage 0.92, 0.96, 0.98, 1.00 V for the control, neoPAI, neoPABr, and neoPACI samples, respectively). d) Images of water droplets on the surface of 3D pristine and LDP-passivated perovskite films. e) High-resolution C 1s core level of perovskite films without and with the passivation of neoPAI, neoPABr, and neoPACI treatment. f) Comparing of long-term stability tests on the unencapsulated devices under $\sim 20\%$ RH at room temperature.

transfer occurs between the surface $n = 2$ perovskite phases and the 3D bulk. Ultimately, while we observe improvements in all films prepared using a large organic-spacer salt treatment, the formation of a quasi-2D/3D heterojunction upon treatment with neoPACI enables suppressed interfacial charge recombination, remarkable energy transfer enhancement and a PCE over 23%. Furthermore, we show evidence of optimal environmental stability when preparing devices using a Cl-based salt. We thus find the choice of halide for conducting 2D/quasi-2D passivation treatments is equally important to that of the large cation and should be carefully considered. This work has a profound meaning for the deeper understanding of the role of halide anions in low-dimensional phases formation, which provide design criteria for further low-dimensional perovskite quasi-2D/3D heterojunctions for a range of photovoltaic and optoelectronic applications.

4. Experimental Section

Materials: Lead iodide (PbI_2 , 99.99%) was purchased from Tokyo Chemical Industry Co., Ltd (TCI). Formamidinium iodide (FAI), methylammonium iodide (MAI), methylamine hydrochloride (MACl), neo-pentylammonium iodide (neoPAI), neo-pentylammonium bromide (neoPABr), and neo-pentylammonium chloride (neoPACI) were purchased from GreatCell Solar. SnO_2 colloid precursor solution (tin(IV) oxide, 15% in H_2O colloidal dispersion) was obtained from Alfa Aesar. Lithium Bis(trifluoromethanesulfonyl)imide salt (Li-TFSI) and 4-tert-butylpyridine (tBP) were obtained from Sigma-Aldrich. 2,2',7,7'-Tetrakis(N,N-di-p-methoxyphenylamino)-9,9'-spirobifluorene (Spiro-OMeTAD, LT-S922), tris(2-(1H-pyrazol-1-yl)-4-tert-butylpyridine)-cobalt(III)tris(bis(trifluoromethylsulfonyl)imide)

(FK209) were purchased from Xi'an Polymer Light Technology. The solvents used including isopropanol (IPA, 99.5%), N,N-dimethylformamide (DMF, 99.8%), dimethyl sulfoxide (DMSO, 99.7%), chlorobenzene (99.8%), acetonitrile (ACN, 99.9%) were purchased from Sigma-Aldrich and without further purification.

Perovskite devices fabrication: The PSCs were fabricated with a planar structure of $\text{ITO}/\text{SnO}_2/\text{perovskite}/\text{Spiro-OMeTAD}/\text{Au}$. The ITO glass substrate was cleaned sequentially with Hellmanex™ cleaning solution (diluted with water to 2%), deionized water, acetone, and isopropyl alcohol (IPA) in an ultrasonic bath for 20 min. Before SnO_2 deposition, the ITO substrate was treated by ultraviolet-ozone cleaner for 15 min. Then the diluted SnO_2 (V_{SnO_2} colloidal dispersion; $\text{V}_{\text{water}} = 1:5$) nanocrystal solution was spin-coated on the cleaned substrate at 3000 r.p.m. for 30 s, followed by annealing at 150°C for 30 min in air environment (30–50% RH). The SnO_2 films were treated with ultraviolet-ozone for 15 min before being transferred to the nitrogen glove box. The perovskite absorber films were fabricated by two-step solution process: 1.3 M PbI_2 solutions dissolved in DMF/DMSO mixed solvent ($\text{V}_{\text{DMF}}:\text{V}_{\text{DMSO}} = 9:1$) and stirring overnight before use. The PbI_2 films were fabricated by spin-coating PbI_2 precursor solution onto SnO_2 substrate at the speed of 1500 r.p.m. for 30 s and then annealed at 70°C for 1 min in the nitrogen glove box. FAI/MAI/MACl mixed organic components were prepared by dissolving 60 mg FAI, 6 mg MAI and 6 mg MACl in 1 mL IPA solvent, then spin-coated onto the PbI_2 films at 1600 r.p.m. for 30 s. The intermediate phase film was put on a hotplate at 150°C for 15 min in air environment. After the substrate cooling down, the perovskite film was spin-coated with 25 mM neo-pentylammonium iodide (neoPAI), neo-pentylammonium bromide (neoPABr) and neo-pentylammonium chloride (neoPACI) solution (dissolved in IPA) at 3000 r.p.m., then annealed at 100°C for 5 min. The hole transfer materials were prepared by dissolving 90 mg Spiro-OMeTAD in 1 mL chlorobenzene solvent and then 35 mL tBP, 23 mL Li-TFSI (520 mg mL^{-1} in acetonitrile), and 10 μL FK209 (300 mg mL^{-1} in acetonitrile) were added. Subsequently, Spiro-OMeTAD solution was deposited onto the

perovskite film at 4000 r.p.m. for 20 s. Finally, 100 nm Au electrode was thermally evaporated on hole-transporting layer to complete the whole devices. The 2D perovskite films of (neoPA)₂PbI₄, (neoPA)₂PbBr₄, (neoPA)₂PbCl₄, and (neoPA)₂(FA)Pb₂I₇ for XRD measurement are prepared by dissolving 1 M PbI₂ and neoPAX powders in stoichiometric ratio in DMF/DMSO mixed solvent ($V_{\text{DMF}}:V_{\text{DMSO}} = 9:1$). 20 mg mL⁻¹ (in CB) PCBM was spun onto the perovskite layer at 1500 r.p.m. for 30 s with a ramping rate of 500 r.p.m. s⁻¹ for preparing electron-only devices with the structure of ITO/SnO₂/perovskite/PCBM/Au.

GIWAX characterization: Grazing incidence wide-angle X-ray scattering (GIWAXS) was collected using a Xeuss 2.0 system (XENOCSS) with 9.243 keV ($\lambda = 1.3414 \text{ \AA}$) photons produced from a Ga Metaljet (EXCILLUM) source. X-rays were then directed onto the sample surface at grazing incidence angles (α_i) of 0.2°, 1°, and 2° as indicated. Scattering from the film was detected using a PILATUS3R 1 M detector (DECTRIS) at approximately 300 mm sample to detector distance. The flight tube and sample chamber were held under vacuum to minimize any background scatter. Data were calibrated with an AgBe standard, before being processed and integrated using routines based on the PyFAI and Pygix libraries.^[93] Where shown, equivalent 2θ values were calculated using Cu K α emission of $\lambda = 1.5406 \text{ \AA}$ with the relation $Q = 4\pi \sin(\theta)/\lambda$.

The ultrafast transient reflection spectroscopy characterization: For the transient reflection spectroscopy, the output of a Ti:sapphire amplifier system (Spectra Physics Solstice Ace) operating at 1 kHz and generating ~100-fs pulses was split into two beam paths, pump and probe. The 520- and 720-nm pump pulses were generated in a home-built noncollinear optical parametric amplifier (NOPA), which was blocked by a chopper wheel rotating at 500 Hz. The visible broadband beam (520–780 nm) was generated in a home-built noncollinear optical parametric amplifier (NOPA) while a computer operated a mechanical delay stage (Thorlabs DDS300-E/M) to adjust the delay between the pump and the probe. The white light coming out from the delay stage was split into two identical beams (probe and reference) by a 50/50 beam splitter. The reference beam did not interact with the pump at the sample, which allows for correcting for any shot-to-shot fluctuations. The reflected probe and reference pulses were collected with a silicon dual-line array detector (Hamamatsu S8381-1024Q, spectrograph: Andor Shamrock SR-303i-B) driven and read out by a custom-built board (Stresing Entwicklungsbüro).

Film characterizations: XRD and GIXRD patterns of the films were recorded by X-ray diffractometer PANalytical X'Pert Pro with Cu K α ($\lambda = 0.154187 \text{ nm}$) radiation. The surface and cross-sectional morphologies were acquired by a field emission SEM (Jeol 7100F). AFM images were obtained using a Bruker Multimode 8 scanning probe microscope (tapping mode). Steady-state PL measurement was carried out using an FLS1000 Photoluminescence Spectrometer in which a 450 nm monochromatic laser was used as an excitation fluorescence source. The time-correlated single-photon counting technique was used to count emission photons, which was investigated by confocal microscope setup (PicoQuant, MicroTime 200). Perovskite films were excited by a pulsed diode (PDL 828, PicoQuant, pulse width ~100 ps) with an air objective. The signals were focused onto a Hybrid PMT detector connected to a Picoquant acquisition card for time-correlated single-photon counting with a time resolution of 200 ps. UV-visible absorption spectra of perovskite films were performed by Varian Cary 5000 UV-vis-NIR spectrophotometer, in which monochromatic light was incident to the substrate side. ToF-SIMS depth profile analysis was conducted using an TOF.SIMS 5 system, ION-TOF GmbH (Münster, Germany). XPS measurement was performed on a ThermoFisher Scientific Instruments (East Grinstead, UK) with a monochromated Al K α X-ray source (1486.6 eV) in a vacuum of 3.0×10^{-8} Torr. Ultraviolet photoelectron spectroscopy was recorded with an Imaging Photoelectron Spectrometer (Axis Ultra, Kratos Analytical Ltd), with a nonmonochromated He I α photon source ($h\nu = 21.22 \text{ eV}$, emission current is 10 mA).

Photovoltaic device characterization: For the whole devices, current–voltage characteristics were recorded under ambient temperature and air conditions. $J-V$ curves were obtained using a Keysight B2901A Source Meter under standard AM 1.5 G illumination (100 mW cm^{-2}) with a solar simulator (Enli Technology Co. Ltd, Taiwan, SS-F5-3A). The light intensity was calibrated by a standard monocrystalline silicon solar cell with a KG-5 filter, and a reference cell was purchased from Fraunhofer ISE Callab (ISE001/013-2018). Both reverse scan (from 1.2 to -0.2 V , step 0.02 V) and forward scan (from -0.2 to 1.2 V, step 0.02 V) were carried out with a delay time of 100 ms. The active area was determined by

a 0.09 cm^2 metal mask placed in front of the solar cell. EQE spectra were measured using an internal quantum efficiency system (Bentham PV300) under irradiation by a 100 W Xenon lamp ranging from 300 to 850 nm.

Acknowledgements

X.L. and T.W. are contributed equally to this work. W. Z. acknowledges the Engineering and Physical Sciences Research Council (EPSRC) New Investigator Award (2018; EP/R043272/1), and Marie Skłodowska-Curie Actions Individual Fellowships (839136). H. L. acknowledges the Newton Advanced Fellowship (192097). X. L. acknowledges the financial support from Zhengzhou University Scholarship. T.W. thanks the University of Surrey Doctoral College for financial support. S.J.S. gratefully acknowledges the support of EPSRC (UK) under grant number EP/N021037/1. L. D. thanks the China Scholarship Council and the Cambridge Trusts for funding. R. C. K. and J. A. S. thank the company Xenocs for their ongoing support through the X-ray scattering user program at the University of Sheffield and the EPSRC for funding the purchase of this instrument. Z. W., Y. S., and G. S. thank the financial support from Zhengzhou Materials Genome Institute. S. D. S. and K. J. acknowledge the Royal Society for funding.

Conflicts of Interest

S. D. S. is a co-founder of Swift Solar. The other authors declare no competing interests.

Author Contributions

X. L. conceived the ideas and designed the project with the directed and supervised by W. Z. and S. R. P. X. L. and M. Y. carried out solar cell fabrication. X. L. performed EQE, UV-vis, SEM, and SCLC characterization. T. W. and J. B. performed XRD and GIXRD measurements. L. D. carried out the transient reflection spectroscopy and analyzed the data under the supervision of N. C. G. T. W. conducted AFM and contact angle measurements. T. W. and A. R. performed PL measurement. K. J. carried out TCSPC characterizations. R. C. K. conducted the GIWAXS measurement. J. A. S. analyzed the GIWAXS data. S. H. assisted with XPS and ToF-SIMS measurements. Y. S. conducted UPS measurement. X. L. analyzed the data and wrote the manuscript, W. Z., T. W. and J. A. S. revised the manuscript. All authors were involved in the discussion of data analysis and commented on the manuscript.

Supporting Information

Supporting Information is available from the Wiley Online Library or from the author.

Keywords

carrier dynamics, halide anions (I, Br, Cl), neo-pentylammonium halides, perovskite solar cells, quasi-2D/3D heterojunction

Received: September 19, 2021

Revised: October 30, 2021

Published online: November 27, 2021

[1] National Renewable Energy Laboratory, Best Research-Cell Efficiencies, <https://www.nrel.gov/pv/assets/pdfs/best-research-cell-efficiencies.20200925.pdf> (accessed: September 2020).

[2] A. K. Jena, A. Kulkarni, T. Miyasaka, *Chem. Rev.* **2019**, 119, 3036.

- [3] S. Tan, I. Yavuz, M. H. Weber, T. Y. Huang, C. H. Chen, R. Wang, H. C. Wang, J. H. Ko, S. Nuryyeva, J. J. Xue, Y. P. Zhao, K. H. Wei, J. W. Lee, Y. Yang, *Joule* **2020**, 4, 2426.
- [4] L. G. Wang, H. P. Zhou, J. N. Hu, B. L. Huang, M. Z. Sun, B. W. Dong, G. H. J. Zheng, Y. Huang, Y. H. Chen, L. Li, Z. Q. Xu, N. X. Li, Z. Liu, Q. Chen, L. D. Sun, C. H. Yan, *Science* **2019**, 363, 265.
- [5] M. Stolterfoht, M. Grischek, P. Caprioglio, C. M. Wolff, E. Gutierrez-Partida, F. Pena-Camargo, D. Rothhardt, S. S. Zhang, M. Raoufi, J. Wolansky, M. Abdi-Jalebi, S. D. Stranks, S. Albrecht, T. Kirchartz, D. Neher, *Adv. Mater.* **2020**, 32, 10.
- [6] F. Gao, Y. Zhao, X. W. Zhang, J. B. You, *Adv. Energy Mater.* **2020**, 10, 30.
- [7] D. Shi, V. Adinolfi, R. Comin, M. J. Yuan, E. Alarousu, A. Buin, Y. Chen, S. Hoogland, A. Rothenberger, K. Katsiev, Y. Losovyj, X. Zhang, P. A. Dowben, O. F. Mohammed, E. H. Sargent, O. M. Bakr, *Science* **2015**, 347, 519.
- [8] S. Mahesh, J. M. Ball, R. D. J. Oliver, D. P. McMeekin, P. K. Nayak, M. B. Johnston, H. J. Snaith, *Energy Environ. Sci.* **2020**, 13, 258.
- [9] T. A. S. Doherty, A. J. Winchester, S. Macpherson, D. N. Johnstone, V. Pareek, E. M. Tennyson, S. Kosar, F. U. Kosasih, M. Anaya, M. Abdi-Jalebi, Z. Andaji-Garmaroudi, E. L. Wong, J. Madeo, Y. H. Chiang, J. S. Park, Y. K. Jung, C. E. Petoukhoff, G. Divitini, M. K. L. Man, C. Ducati, A. Walsh, P. A. Midgley, K. M. Dani, S. D. Stranks, *Nature* **2020**, 580, 360.
- [10] C. Eames, J. M. Frost, P. R. F. Barnes, B. C. O'Regan, A. Walsh, M. S. Islam, *Nat. Commun.* **2015**, 6, 8.
- [11] T. Leijtens, G. E. Eperon, A. J. Barker, G. Grancini, W. Zhang, J. M. Ball, A. R. S. Kandada, H. J. Snaith, A. Petrozza, *Energy Environ. Sci.* **2016**, 9, 3472.
- [12] L. K. Ono, S. Z. Liu, Y. B. Qi, *Angew. Chem. Int. Edit.* **2020**, 59, 6676.
- [13] A. Walsh, D. O. Scanlon, S. Y. Chen, X. G. Gong, S. H. Wei, *Angew. Chem. Int. Edit.* **2015**, 54, 1791.
- [14] T. A. Berhe, W. N. Su, C. H. Chen, C. J. Pan, J. H. Cheng, H. M. Chen, M. C. Tsai, L. Y. Chen, A. A. Dubale, B. J. Hwang, *Energy Environ. Sci.* **2016**, 9, 323.
- [15] M. I. Saidaminov, J. Kim, A. Jain, R. Quintero-Bermudez, H. R. Tan, G. K. Long, F. R. Tan, A. Johnston, Y. C. Zhao, O. Voznyy, E. H. Sargent, *Nature Energy* **2018**, 3, 648.
- [16] R. Wang, J. J. Xue, L. Meng, J. W. Lee, Z. P. Zhao, P. Y. Sun, L. Cai, T. Y. Huang, Z. X. Wang, Z. K. Wang, Y. Duan, J. L. Yang, S. Tan, Y. Yuan, Y. Huang, Y. Yang, *Joule* **2019**, 3, 1464.
- [17] Y. P. Zhao, P. C. Zhu, M. H. Wang, S. Huang, Z. P. Zhao, S. Tan, T. H. Han, J. W. Lee, T. Y. Huang, R. Wang, J. J. Xue, D. Meng, Y. Huang, J. Marian, J. Zhu, Y. Yang, *Adv. Mater.* **2020**, 32, 8.
- [18] M. Saliba, T. Matsui, J. Y. Seo, K. Domanski, J. P. Correa-Baena, M. K. Nazeeruddin, S. M. Zakeeruddin, W. Tress, A. Abate, A. Hagfeldt, M. Gratzel, *Energy Environ. Sci.* **1989**, 2016, 9.
- [19] G. Kim, H. Min, K. S. Lee, D. Y. Lee, S. M. Yoon, S. I. Seok, *Science* **2020**, 370, 108.
- [20] Q. Jiang, Y. Zhao, X. W. Zhang, X. L. Yang, Y. Chen, Z. M. Chu, Q. F. Ye, X. X. Li, Z. G. Yin, J. B. You, *Nat. Photonics* **2019**, 13, 460.
- [21] T. Q. Niu, J. Lu, R. Munir, J. B. Li, D. Barrit, X. Zhang, H. L. Hu, Z. Yang, A. Amassian, K. Zhao, S. Z. Liu, *Adv. Mater.* **2018**, 30, 11.
- [22] Y. H. Shao, Z. G. Xiao, C. Bi, Y. B. Yuan, J. S. Huang, *Nat. Commun.* **2014**, 5, 7.
- [23] X. P. Zheng, B. Chen, J. Dai, Y. J. Fang, Y. Bai, Y. Z. Lin, H. T. Wei, X. C. Zeng, J. S. Huang, *Nat. Energy* **2017**, 2, 9.
- [24] Y. C. Shao, Y. B. Yuan, J. S. Huang, *Nat. Energy* **2016**, 1, 6.
- [25] D. Y. Luo, W. Q. Yang, Z. P. Wang, A. Sadhanala, Q. Hu, R. Su, R. Shivan, G. F. Trindade, J. F. Watts, Z. J. Xu, T. H. Liu, K. Chen, F. J. Ye, P. Wu, L. C. Zhao, J. Wu, Y. G. Tu, Y. F. Zhang, X. Y. Yang, W. Zhang, R. H. Friend, Q. H. Gong, H. J. Snaith, R. Zhu, *Science* **2018**, 360, 1442.
- [26] E. H. Jung, N. J. Jeon, E. Y. Park, C. S. Moon, T. J. Shin, T. Y. Yang, J. H. Noh, J. Seo, *Nature* **2019**, 567, 511.
- [27] M. Kim, G. H. Kim, T. K. Lee, I. W. Choi, H. W. Choi, Y. Jo, Y. J. Yoon, J. W. Kim, J. Lee, D. Huh, H. Lee, S. K. Kwak, J. Y. Kim, D. S. Kim, *Joule* **2019**, 3, 2179.
- [28] F. H. Ye, J. J. Ma, C. Chen, H. B. Wang, Y. H. Xu, S. P. Zhang, T. Wang, C. Tao, G. J. Fang, *Adv. Mater.* **2021**, 33, 2007126.
- [29] W. S. Yang, B. W. Park, E. H. Jung, N. J. Jeon, Y. C. Kim, D. U. Lee, S. S. Shin, J. Seo, E. K. Kim, J. H. Noh, S. I. Seok, *Science* **2017**, 356, 1376.
- [30] B. W. Park, N. Kedem, M. Kulbak, D. Y. Lee, W. S. Yang, N. J. Jeon, J. Seo, G. Kim, K. J. Kim, T. J. Shin, G. Hodes, D. Cahen, S. I. Seok, *Nat. Commun.* **2018**, 9, 8.
- [31] T. H. Han, J. W. Lee, C. Choi, S. Tan, C. Lee, Y. P. Zhao, Z. H. Dai, N. De Marco, S. J. Lee, S. H. Bae, Y. H. Yuan, H. M. Lee, Y. Huang, Y. Yang, *Nat. Commun.* **2019**, 10, 10.
- [32] Y. H. Liu, S. Akin, A. Hinderhofer, F. T. Eickemeyer, H. W. Zhu, J. Y. Seo, J. H. Zhang, F. Schreiber, H. Zhang, S. M. Zakeeruddin, A. Hagfeldt, M. I. Dar, M. Gratzel, *Angew. Chem. Int. Edit.* **2020**, 59, 15688.
- [33] J. Jeong, M. Kim, J. Seo, H. Z. Lu, P. Ahlawat, A. Mishra, Y. G. Yang, M. A. Hope, F. T. Eickemeyer, M. Kim, Y. J. Yoon, I. W. Choi, B. P. Darwich, S. J. Choi, Y. Jo, J. H. Lee, B. Walker, S. M. Zakeeruddin, L. Emsley, U. Rothlisberger, A. Hagfeldt, D. S. Kim, M. Gratzel, J. Y. Kim, *Nature* **2021**, 592, 381.
- [34] C. C. Stoumpos, D. H. Cao, D. J. Clark, J. Young, J. M. Rondinelli, J. I. Jang, J. T. Hupp, M. G. Kanatzidis, *Chem. Mat.* **2016**, 28, 2852.
- [35] H. Li, J. Shi, J. Deng, Z. Chen, Y. Li, W. Zhao, J. Wu, H. Wu, Y. Luo, D. Li, Q. Meng, *Adv. Mater.* **2020**, 32, e1907396.
- [36] T. Webb, S. J. Sweeney, W. Zhang, *Adv. Funct. Mater.* **2021**, 31, 2103121.
- [37] S. Yang, J. Dai, Z. H. Yu, Y. C. Shao, Y. Zhou, X. Xiao, X. C. Zeng, J. S. Huang, *J. Am. Chem. Soc.* **2020**, 142, 11937.
- [38] J. F. Lu, L. C. Jiang, W. Li, F. Li, N. K. Pai, A. D. Scully, C. M. Tsai, U. Bach, A. N. Simonov, Y. B. Cheng, L. Piccia, *Adv. Energy Mater.* **2017**, 7, 1700444.
- [39] X. T. Li, J. M. Hoffman, M. G. Kanatzidis, *Chem. Rev.* **2021**, 121, 2230.
- [40] M. Jung, T. J. Shin, J. Seo, G. Kim, S. I. Seok, *Energy Environ. Sci.* **2018**, 11, 2188.
- [41] J. J. Yoo, S. Wiegand, M. C. Sponseller, M. R. Chua, S. N. Bertram, N. T. P. Hartono, J. S. Tresback, E. C. Hansen, J. P. Correa-Baena, V. Bulovic, T. Buonassisi, S. S. Shin, M. G. Bawendi, *Energy Environ. Sci.* **2019**, 12, 2192.
- [42] F. Wang, W. Geng, Y. Zhou, H. H. Fang, C. J. Tong, M. A. Loi, L. M. Liu, N. Zhao, *Adv. Mater.* **2016**, 28, 9986.
- [43] H. Kim, S. U. Lee, D. Y. Lee, M. J. Paik, H. Na, J. Lee, S. I. Seok, *Adv. Energy Mater.* **2019**, 9, 8.
- [44] J. Zhuang, P. Mao, Y. G. Luan, X. H. Yi, Z. Y. Tu, Y. Y. Zhang, Y. P. Yi, Y. Z. Wei, N. L. Chen, T. Lin, F. Y. Wang, C. Li, J. Z. Wang, *ACS Energy Lett.* **2019**, 4, 2913.
- [45] N. De Marco, H. P. Zhou, Q. Chen, P. Y. Sun, Z. H. Liu, L. Meng, E. P. Yao, Y. S. Liu, A. Schiffer, Y. Yang, *Nano Lett.* **2016**, 16, 1009.
- [46] N. X. Li, S. X. Tao, Y. H. Chen, X. X. Niu, C. K. Onwudinanti, C. Hu, Z. W. Qiu, Z. Q. Xu, G. H. J. Zheng, L. G. Wang, Y. Zhang, L. Li, H. F. Liu, Y. Z. Lun, J. W. Hong, X. Y. Wang, Y. Q. Liu, H. P. Xie, Y. L. Gao, Y. Bai, S. H. Yang, G. Brocks, Q. Chen, H. P. Zhou, *Nat. Energy* **2019**, 4, 408.
- [47] M. J. Yang, T. Y. Zhang, P. Schulz, Z. Li, G. Li, D. H. Kim, N. J. Guo, J. J. Berry, K. Zhu, Y. X. Zhao, *Nat. Commun.* **2016**, 7, 9.
- [48] Z. P. Wang, Q. Q. Lin, F. P. Chmiel, N. Sakai, L. M. Herz, H. J. Snaith, *Nat. Energy* **2017**, 2, 17135.
- [49] Y. H. Liu, S. Akin, L. F. Pan, R. Uchida, N. Arora, J. V. Milic, A. Hinderhofer, F. Schreiber, A. R. Uhl, S. M. Zakeeruddin, A. Hagfeldt, M. I. Dar, M. Gratzel, *Sci. Adv.* **2019**, 5, 2543.
- [50] H. Kim, S. U. Lee, D. Y. Lee, M. J. Paik, H. Na, J. Lee, S. I. Seok, *Adv. Energy Mater.* **2019**, 9, 1902740.
- [51] Y. W. Jang, S. Lee, K. M. Yeom, K. Jeong, K. Choi, M. Choi, J. H. Noh, *Nat. Energy* **2021**, 6, 63.
- [52] T. Q. Niu, J. Lu, X. G. Jia, Z. Xu, M. C. Tang, D. Barrit, N. Y. Yuan, J. N. Ding, X. Zhang, Y. Y. Fan, T. Luo, Y. L. Zhang, D. M. Smilgies, Z. K. Liu, A. Amassian, S. Y. Jin, K. Zhao, S. Z. Liu, *Nano Lett.* **2019**, 19, 7181.
- [53] M. Y. Kuo, N. Spitha, M. P. Hautzinger, P. L. Hsieh, J. Li, D. X. Pan, Y. Z. Zhao, L. J. Chen, M. H. Huang, S. Jin, Y. J. Hsu, J. C. Wright, *J. Am. Chem. Soc.* **2021**, 143, 4969.

- [54] X. Jiang, H. Li, Q. Zhou, Q. Wei, M. Wei, L. Jiang, Z. Wang, Z. Peng, F. Wang, Z. Zang, K. Xu, Y. Hou, S. Teale, W. Zhou, R. Si, X. Gao, E. H. Sargent, Z. Ning, *J. Am. Chem. Soc.* **2021**, 143, 10970.
- [55] J. J. Yoo, G. Seo, M. R. Chua, T. G. Park, Y. L. Lu, F. Rotermund, Y. K. Kim, C. S. Moon, N. J. Jeon, J. P. Correa-Baena, V. Bulovic, S. S. Shin, M. G. Bawendi, J. Seo, *Nature* **2021**, 590, 587.
- [56] Y. Lin, Y. Bai, Y. J. Fang, Z. L. Chen, S. Yang, X. P. Zheng, S. Tang, Y. Liu, J. J. Zhao, J. S. Huang, *J. Phys. Chem. Lett.* **2018**, 9, 654.
- [57] S. Yang, Y. C. Zheng, Y. Hou, X. Chen, Y. Chen, Y. Wang, H. J. Zhao, H. G. Yang, *Chem. Mat.* **2014**, 26, 6705.
- [58] R. J. E. Westbrooke, W. D. Xu, X. X. Liang, T. Webb, T. M. Clarke, S. A. Haque, *J. Phys. Chem. Lett.* **2021**, 12, 3312.
- [59] E. I. Marchenko, S. A. Fateev, A. A. Petrov, V. V. Korolev, A. Mitrofanov, A. V. Petrov, E. A. Goodilin, A. B. Tarasov, *Chem. Mat.* **2020**, 32, 7383.
- [60] Z. X. Wang, W. Q. Liao, H. Y. Ye, Y. Zhang, *Dalton Trans.* **2015**, 44, 20406.
- [61] R. T. Dong, C. Y. Lan, X. W. Xu, X. G. Liang, X. Y. Hu, D. P. Li, Z. Y. Zhou, L. Shu, S. Yip, C. Li, S. W. Tsang, J. C. Ho, *ACS Appl. Mater. Interfaces* **2018**, 10, 19019.
- [62] I. W. H. Oswald, A. A. Koegel, J. R. Neilson, *Chem. Mat.* **2018**, 30, 8606.
- [63] J. M. Hoffman, C. D. Malliakas, S. Sidhik, I. Hadar, R. McClain, A. D. Mohite, M. G. Kanatzidis, *Chem. Sci.* **2020**, 11, 12139.
- [64] Y. N. Chen, Y. Sun, J. J. Peng, W. Zhang, X. J. Su, K. B. Zheng, T. Pullerits, Z. Q. Liang, *Adv. Energy Mater.* **2017**, 7, 7.
- [65] S. Y. Shao, J. Liu, G. Portale, H. H. Fang, G. R. Blake, G. H. ten Brink, L. J. A. Koster, M. A. Loi, *Adv. Energy Mater.* **2018**, 8, 10.
- [66] F. Wang, X. Y. Jiang, H. Chen, Y. Q. Shang, H. F. Liu, J. L. Wei, W. J. Zhou, H. L. He, W. M. Liu, Z. J. Ning, *Joule* **2018**, 2, 2732.
- [67] Y. L. Yang, F. Lou, H. J. Xiang, *Nano Lett.* **2021**, 21, 3170.
- [68] D. T. Gangadharan, D. L. Ma, *Energy Environ. Sci.* **2019**, 12, 2860.
- [69] D. H. Cao, C. C. Stoumpos, O. K. Farha, J. T. Hupp, M. G. Kanatzidis, *J. Am. Chem. Soc.* **2015**, 137, 7843.
- [70] R. Yang, R. Z. Li, Y. Cao, Y. Q. Wei, Y. F. Miao, W. L. Tan, X. C. Jiao, H. Chen, L. D. Zhang, Q. Chen, H. T. Zhang, W. Zou, Y. M. Wang, M. Yang, C. Yi, N. N. Wang, F. Gao, C. R. McNeill, T. S. Qin, J. P. Wang, W. Huang, *Adv. Mater.* **2018**, 30, 8.
- [71] B. Saparov, D. B. Mitzi, *Chem. Rev.* **2016**, 116, 4558.
- [72] X. Y. Yang, D. Y. Luo, Y. R. Xiang, L. C. Zhao, M. Anaya, Y. L. Shen, J. Wu, W. Q. Yang, Y. H. Chiang, Y. G. Tu, R. Su, Q. Hu, H. Y. Yu, G. S. Shao, W. Huang, T. P. Russell, Q. H. Gong, S. D. Stranks, W. Zhang, R. Zhu, *Adv. Mater.* **2021**, 33, 2006435.
- [73] X. P. Zheng, J. Troughton, N. Gasparini, Y. B. Lin, M. Y. Wei, Y. Hou, J. K. Liu, K. P. Song, Z. L. Chen, C. Yang, B. Turedi, A. Y. Alsalloum, J. Pan, J. Chen, A. A. Zhumekenov, T. D. Anthopoulos, Y. Han, D. Baran, O. F. Mohammed, E. H. Sargent, O. M. Bakr, *Joule* **2019**, 3, 2019.
- [74] T. W. Jones, A. Osherov, M. Alsari, M. Sponseller, B. C. Duck, Y. K. Jung, C. Settens, F. Niroui, R. Brenes, C. V. Stan, Y. Li, M. Abdi-Jalebi, N. Tamura, J. E. Macdonald, M. Burghammer, R. H. Friend, V. Bulovic, A. Walsh, G. J. Wilson, S. Lilliu, S. D. Stranks, *Energy Environ. Sci.* **2019**, 12, 596.
- [75] J. T. W. Wang, Z. P. Wang, S. Pathak, W. Zhang, D. W. deQuilettes, F. Wisnivesky-Rocca-Rivarola, J. Huang, P. K. Nayak, J. B. Patel, H. A. M. Yusof, Y. Vaynzof, R. Zhu, I. Ramirez, J. Zhang, C. Ducati, C. Grovenor, M. B. Johnston, D. S. Ginger, R. J. Nicholas, H. J. Snaith, *Energy Environ. Sci.* **2016**, 9, 2892.
- [76] X. Y. Yang, Y. Q. Fu, R. Su, Y. F. Zheng, Y. Z. Zhang, W. Q. Yang, M. T. Yu, P. Chen, Y. J. Wang, J. Wu, D. Y. Luo, Y. G. Tu, L. C. Zhao, Q. H. Gong, R. Zhu, *Adv. Mater.* **2020**, 32, 8.
- [77] S. H. Zhao, J. S. Xie, G. H. Cheng, Y. R. Xiang, H. Y. Zhu, W. Y. Guo, H. Wang, M. C. Qin, X. H. Lu, J. L. Qu, J. N. Wang, J. B. Xu, K. Y. Yan, *Small* **2018**, 14, 11.
- [78] S. F. Wu, J. Zhang, Z. Li, D. J. Liu, M. C. Qin, S. H. Cheung, X. H. Lu, D. Y. Lei, S. K. So, Z. L. Zhu, A. K. Y. Jen, *Joule* **2020**, 4, 1248.
- [79] I. X. Liu, J. Leng, K. F. Wu, J. Zhang, S. Y. Jin, *J. Am. Chem. Soc.* **2017**, 139, 1432.
- [80] P. R. Cheng, P. J. Wang, Z. Xu, X. G. Jia, Q. L. Wei, N. Y. Yuan, J. N. Ding, R. P. Li, G. T. Zhao, Y. C. Cheng, K. Zhao, S. Z. R. Liu, *ACS Energy Lett.* **2019**, 4, 4.
- [81] Y. L. Zhang, P. J. Wang, M. C. Tang, D. Barrit, W. J. Ke, J. X. Liu, T. Luo, Y. C. Liu, T. Q. Niu, D. M. Smilgies, Z. Yang, Z. K. Liu, S. Y. Jin, M. G. Kanatzidis, A. Arnassian, S. Z. F. Liu, K. Zhao, *J. Am. Chem. Soc.* **2019**, 141, 2684.
- [82] D. Y. Son, J. W. Lee, Y. J. Choi, I. H. Jang, S. Lee, P. J. Yoo, H. Shin, N. Ahn, M. Choi, D. Kim, N. G. Park, *Nat. Energy* **2016**, 1, 8.
- [83] H. S. Li, J. J. Shi, J. Deng, Z. J. Chen, Y. M. Li, W. Y. Zhao, J. H. Wu, H. J. Wu, Y. H. Luo, D. M. Li, Q. B. Meng, *Adv. Mater.* **2020**, 32, 1907396.
- [84] T. H. Wu, Y. B. Wang, X. Li, Y. Z. Wu, X. Y. Meng, D. Y. Cui, X. D. Yang, L. Y. Han, *Adv. Energy Mater.* **2019**, 9, 1803766.
- [85] Y. F. Qingfeng Dong, Y. Shao, P. Mulligan, J. Qiu, L. Cao, J. Huang, *Science* **2015**, 347, 967.
- [86] C. Liang, H. Gu, Y. D. Xia, Z. Wang, X. T. Liu, J. M. Xia, S. W. Zuo, Y. Hu, X. Y. Gao, W. Hui, L. F. Chao, T. T. Niu, M. Fang, H. Lu, H. Dong, H. Yu, S. Chen, X. Q. Ran, L. Song, B. X. Li, J. Zhang, Y. Peng, G. S. Shao, J. P. Wang, Y. H. Chen, G. C. Xing, W. Huang, *Nat. Energy* **2021**, 6, 38.
- [87] Y. Yang, M. J. Yang, D. T. Moore, Y. Yan, E. M. Miller, K. Zhu, M. C. Beard, *Nat. Energy* **2017**, 2, 7.
- [88] D. Y. Luo, R. Su, W. Zhang, Q. H. Gong, R. Zhu, *Nat. Rev. Mater.* **2020**, 5, 44.
- [89] G. C. Xing, N. Mathews, S. Y. Sun, S. S. Lim, Y. M. Lam, M. Gratzel, S. Mhaisalkar, T. C. Sum, *Science* **2013**, 342, 344.
- [90] Q. Sun, P. Fassi, D. Becker-Koch, A. Bausch, B. Rivkin, S. Bai, P. E. Hopkinson, H. J. Snaith, Y. Vaynzof, *Adv. Energy Mater.* **2017**, 7, 10.
- [91] H. W. Zhu, Y. H. Liu, F. T. Eickemeyer, L. F. Pan, D. Ren, M. A. Ruiz-Preciado, B. Carlsen, B. W. Yang, X. F. Dong, Z. W. Wang, H. L. Liu, S. R. Wang, S. M. Zakeeruddin, A. Hagfeldt, M. I. Dar, X. G. Li, M. Gratzel, *Adv. Mater.* **2020**, 32, 8.
- [92] M. V. Khenkin, E. A. Katz, A. Abate, G. Bardizza, J. J. Berry, C. Brabec, F. Brunetti, V. Bulovic, Q. Burlingame, A. Di Carlo, R. Cheacharoen, Y. B. Cheng, A. Colmann, S. Cros, K. Domanski, M. Dusza, C. J. Fell, S. R. Forrest, Y. Galagan, D. Di Girolamo, M. Graetzel, A. Hagfeldt, E. von Hauff, H. Hoppe, J. Kettle, H. Koebler, M. S. Leite, S. Liu, Y. L. Loo, J. M. Luther, C. Q. Ma, M. Madsen, M. Manceau, M. Matheron, M. McGehee, R. Meitzner, M. K. Nazeeruddin, A. F. Nogueira, C. Odabasi, A. Osherov, N. G. Park, M. O. Reese, F. De Rossi, M. Saliba, U. S. Schubert, H. J. Snaith, S. D. Stranks, W. Tress, P. A. Troshin, V. Turkovic, S. Veenstra, I. Visoly-Fisher, A. Walsh, T. Watson, H. B. Xie, R. Yildirim, S. M. Zakeeruddin, K. Zhu, M. Lira-Cantu, *Nat. Energy* **2020**, 5, 35.
- [93] G. Ashiotis, A. Deschilde, Z. Nawaz, J. P. Wright, D. Karkoulis, F. E. Picca, J. Kieffer, *J. Appl. Crystallogr.* **2015**, 48, 510.